J. Fluid Mech. (2022), *vol*. 953, A36, doi:10.1017/jfm.2022.954

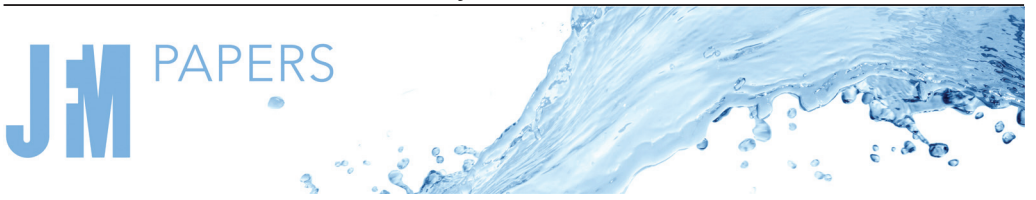

Axisymmetric displacement flows in fluid-driven fractures

Sri Savya Tanikella[1] **and Emilie Dressaire**[1],†

[1]Department of Mechanical Engineering, University of California Santa Barbara, Santa Barbara, CA 93106, USA

(Received 8 June 2022; revised 28 September 2022; accepted 3 November 2022)

Displacement flows are common in hydraulic fracturing, as fracking fluids of different composition are injected sequentially in the fracture. The injection of an immiscible fluid at the centre of a liquid-filled fracture results in the growth of the fracture and the outward displacement of the interface between the two liquids. We study the dynamics of the fluid-driven fracture, which is controlled by the competition between viscous, elastic and toughness-related stresses. We use a model experiment to characterize the dynamics of the fracture for a range of mechanical properties of the fractured material and fracturing fluids. We form the liquid-filled pre-fracture in an elastic brittle matrix of gelatin. The displacing liquid is then injected. We record the radius and aperture of the fracture, and the position of the interface between the two liquids. In a typical experiment, the axisymmetric radial viscous flow is accommodated by the elastic deformation and fracturing of the matrix. We model the coupling between elastic deformation, viscous dissipation and fracture propagation, and recover the two fracturing regimes identified for single-fluid injection. For the viscous-dominated and toughness-dominated regimes, we derive scaling equations that describe the crack growth due to a displacement flow and show the influence of the pre-existing fracture on the crack dynamics through a finite initial volume and an average viscosity of the fluids in the fracture.

Key words: flow-structure interactions, multiphase flow

1. Introduction

Fluid-driven or hydraulic fracturing results from the injection of a pressurized fluid in low-permeability solid media. The formation and propagation of the fluid-filled tensile fracture is observed commonly in engineering and natural geophysical processes. For example, the formation of magma-driven dykes is due to density differences that generate pressure large enough to propagate a vertical fracture in the surrounding rock (Lister &

† Email address for correspondence: dressaire@ucsb.edu

Kerr 1991; Rubin 1995). The most common industrial application of hydraulic fracturing is well stimulation to facilitate the extraction of oil and gas from shale formations (Cueto-Felgueroso & Juanes 2013). A fluid is injected at high pressure to expand fractures initiated with small-scale explosions in unconventional reservoirs. The fractures create new flow pathways, facilitating fluid transport and storage in low-permeability and low-porosity rock formations. Other applications leverage the enhanced transport. For example, fractures connecting wells can be used to extract geothermal energy as the fluid pumped through the fracture heats up when it travels underground (Murphy *et al.* 1981; Caulk *et al.* 2016; Luo *et al.* 2017). Fractures are also used for storage, including carbon sequestration (Huppert & Neufeld 2013; Jia, Tsau & Barati 2019) and disposal of liquid waste (Bao & Eaton 2016; Alessi *et al.* 2017).

The complex mechanics of fluid-driven fractures are controlled by the deforming boundary, fluid flow and stress singularity at the tip of the tensile fracture (Detournay 2016). Field testing, laboratory-scale experiments and predictive modelling evidence that the fracture propagation is characterized by multiple length and time scales. When a Newtonian fluid is injected from a point source, in an infinite, homogeneous and impermeable medium, a single fracture propagates radially. The elastic stress in the medium leads to the growth of a penny-shaped fluid-filled fracture in the direction of minimum confining stress. The propagation of such fractures has been studied extensively as it is essential to the modelling of more complex geological situations, including those involving a finite medium (Bunger & Detournay 2005), complex fluids (Barbati *et al.* 2016; Hormozi & Frigaard 2017; Lai *et al.* 2018) and interacting fractures (O'Keeffe *et al.* 2018*b*). Seminal work on the stress distribution in a penny-shaped fracture (Sneddon & Mott 1946) and the injection of viscous fluids to form fractures (Khristianovic & Zheltov 1955; Barenblatt 1956) led to the development of self-similar solutions for fractures whose propagation is limited by the viscous dissipation in the fluid (Spence & Sharp 1985). Further work on the vicinity of the crack front or tip region identified two asymptotic regimes for the tip geometry and fracture propagation (Desroches *et al.* 1994; Garagash & Detournay 2000, 2005; Savitski & Detournay 2002; Detournay & Garagash 2003). In the viscous-dominated scaling, the viscous dissipation in the flow opposes the elastic stress of the deformable boundary to control the fracture evolution. In the toughness-dominated regime, the material toughness opposes the elasticity-driven propagation of the fracture and determines the system's behaviour. Laboratory-scale experiments commonly rely on clear brittle elastic gels to study the crack tip region and the penny-shaped fracture (Takada 1990; Giuseppe *et al.* 2009; Kavanagh, Menand & Daniels 2013; Baumberger & Ronsin 2020). Injections of water, glycerol and oil in gelatin and polyacrylamide have validated the existence of two propagation regimes and the corresponding scaling laws (Lai *et al.* 2015, 2016; O'Keeffe, Huppert & Linden 2018*a*). The behaviour of the crack tip region was studied by injecting liquid between two plates of polymethylmethacrylate (PMMA) glued by an adhesive (Bunger & Detournay 2008).

Most hydraulic fracturing processes involve multiphase flows and, in particular, displacement flows (Hormozi & Frigaard 2017; Osiptsov 2017; Lai *et al.* 2018; Wang, Elsworth & Denison 2018; Bessmertnykh, Dontsov & Ballarini 2021). During hydraulic fracturing operations, several fluids are injected, ranging from low-viscosity fluids to high-viscosity polymer solutions (Moukhtari & Lecampion 2018; Bessmertnykh *et al.* 2021) and proppant slurries (Hormozi & Frigaard 2017; Wang *et al.* 2018; Barboza, Chen & Li 2021). This sequence of injections aims at increasing the surface area of the fracture and at keeping the fracture open during the hydrocarbon extraction. For example, carbon dioxide injection is a promising strategy to enhance oil recovery after primary production of shale oil reservoirs (Huppert & Neufeld 2013; Jia *et al.* 2019). The rapid injection of

supercritical CO_2 in water-filled fractures is followed by the slower permeation of CO_2 into the rock and the migration of the oil into the fracture. This strategy increases the amount of oil recovered while storing carbon in the rock. Finally, enhanced geothermal systems rely on fractures in hot rocks to connect the injection and extraction wells (Murphy *et al.* 1981; Caulk *et al.* 2016; Parisio & Yoshioka 2020). Fracturing fluids are injected first, and then the working fluid, commonly water or CO_2, is pumped into the fracture to extract heat.

Displacement flows in porous media can give rise to complex out-of-equilibrium flow patterns when the invading fluid has a lower viscosity than the fluid that occupies the porous medium, and is referred to as the displaced or defending fluid. Practically, the patterns generated by liquid–liquid or gas–liquid displacement flows lead to preferential flow pathways in the porous medium. Extensive work has therefore been dedicated to the formation and geometry of the patterns, ranging from experimental to numerical and theoretical (Saffman & Taylor 1958; Paterson 1981; Park & Homsy 1984; Homsy 1987; Lenormand, Touboul & Zarcone 1988; Chen 1989; Tanveer 1993; Primkulov *et al.* 2019). Viscous and capillary forces can contribute to fluid/fluid displacement in a porous medium. A displacement flow is characterized by two dimensionless parameters: the viscosity or mobility ratio $M = \mu_{inv}/\mu_{def}$, and the capillary number of the invading fluid $Ca = \mu_{inv}u/\gamma$, where μ_{inv} and μ_{def} are the viscosities of the invading and defending fluids, respectively, u is the characteristic velocity, and γ is the surface tension of the interface between the two fluids. The influence of the two dimensionless parameters on the geometry of the invading front is summarized in Lenormand's phase diagram (Lenormand *et al.* 1988), which was revisited recently by Primkulov *et al.* (2021) to include wettability. In summary, for large Ca, the viscous forces control the system dynamics and the interfacial forces are negligible. If the invading fluid is more viscous than the defending fluid ($M \geq 1$), then a compact front or interface moves through the porous medium. If the invading fluid is less viscous than the defending one ($M \ll 1$), then the Saffman–Taylor instability leads to an unstable front with the formation of a viscous fingering pattern, observed in porous media of different complexity, from Hele-Shaw cells (Saffman & Taylor 1958; Tabeling, Zocchi & Libchaber 1987) to intricate networks of pores and throats (Lenormand, Zarcone & Sarr 1983; Zhao, MacMinn & Juanes 2016). For low Ca, the interfacial forces contribute to the system dynamics and result in more complex patterns at the interface between the two fluids, depending on the local pore geometry and wettability (Stokes *et al.* 1986; Cottin, Bodiguel & Colin 2010). The rich dynamics of displacement flows is reported in various model porous media, including networks of microchannels and rough fractures (Glass, Rajaram & Detwiler 2003; Chen *et al.* 2017; Yang *et al.* 2019). Yet the system geometry can delay the onset of viscous fingers and even suppress the Saffman–Taylor instability. In a converging Hele-Shaw cell, the stability of the interface depends on the mobility ratio, but also the characteristic velocity, the gradient of cell depth, and the contact angle at the interface (Al-Housseiny, Tsai & Stone 2012; Al-Housseiny & Stone 2013; Lu *et al.* 2019). Below a critical capillary number, a compact front is observed in a converging Hele-Shaw cell despite the unfavourable nature of the displacement. Similar results are reported in flexible cells, whose geometry depends on elastohydrodynamic interactions, such as displacement flows under elastic membranes (Pihler-Puzović *et al.* 2012, 2013, 2015; Peng *et al.* 2015). Two physical mechanisms contribute to the stabilization of the interface under an elastic membrane that deforms as fluid is injected. First, the local increase in cell depth leads to a depth gradient that has been shown to delay viscous fingering for rigid converging cells. Second, the increase in depth reduces the characteristic velocity or capillary number corresponding to a given injection flow rate.

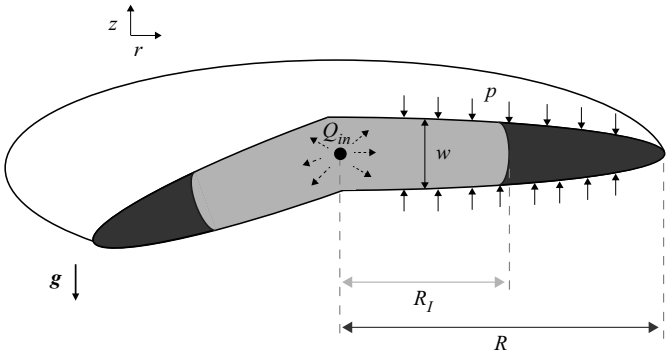

Figure 1. Schematic of a penny-shaped fracture formed by successively injecting two liquids, first the outer fluid (dark grey) and then the inner fluid (light grey). The fracture is axisymmetric.

The purpose of the present paper is to model axisymmetric two-phase flows in fluid-filled growing fractures. Experiments and theoretical modelling focus on immiscible two-phase flows with a mobility ratio smaller than or of order 1 and a low capillary number, ensuring the propagation of a compact front. We build on the approach of Savitski & Detournay (2002) to study the coupling between the two-phase flow and the fracture growth, in the viscous and toughness regimes (§ 2). We derive new scalings for the radius and aperture of the fracture and the position of the interface for immiscible displacement flows in elastic, brittle and impermeable media (§ 3). To test the scalings, we conduct injection experiments in gelatin, which is a common model medium (§ 4). During the two consecutive injections, we record the geometrical parameters of the fracture and compare their time dependence with scalings (§ 5). Finally, we discuss the time scales of the fracturing displacement flow (§ 6).

2. Theoretical models

In this section, we model the displacement flow that is responsible for the propagation of a crack during the successive injections of two immiscible fluids. The mathematical models presented build on the framework introduced originally by Spence & Sharp (1985) and further developed in recent studies of single-fluid injection (Savitski & Detournay 2002; Lai *et al.* 2015; O'Keeffe *et al.* 2018*a*). Past work has focused on the injection of a single incompressible fluid in an elastic brittle solid through a point source (see figure 1), forming a penny-shaped crack. The fracture dynamics depends on the material properties, such as the Young's modulus E, Poisson's ratio ν and toughness K_{IC}, and the injection parameters, i.e. the constant flow rate Q and liquid viscosity μ. As the injection stops, the fracture reaches its final configuration and volume V_0.

This study addresses the injection of an immiscible liquid in a pre-formed penny-shaped crack. The fluid is injected through the same point source at the centre of the crack. The displaced fluid fills an outer annular region of the fracture (see figure 1). In what follows, we use the subscript 'in' to refer to the injected liquid and '0' to refer to the displaced fluid. The surface tension of the interface is denoted γ, and the contact angle with the solid is denoted θ. Over the time scale of an experiment, typically a few minutes, the solid is not porous to the liquids, and the volume of the fracture is equal to the total volume of fluid injected.

We make assumptions regarding fluid flow and fracture propagation to model the system dynamics. As the injection rates are low, we assume that the fracture propagates at equilibrium, and the liquid and fracture fronts coincide at all times, with no fluid lag. The fluid injection results in linear elastic deformation of the surrounding material.

To describe the crack aperture $w(r, t)$, radius $R(t)$ and pressure $p(r, t)$, as well as the position of the interface R_I, we need to solve the coupled equations that describe (*a*) the viscous flow of the two fluid phases in the time-dependent fracture, (*b*) the elastic deformation of the solid material or fracture walls, (*c*) the stress intensity factor at the tip of the fracture, and (*d*) the volume conservation. These sets of equations are coupled by the net pressure in the fracture. The fluid domain is divided into two regions. The outer region is composed of the displaced fluid and bound by the liquid–liquid interface at $r = R_I$ and the crack tip at $r = R$. The injected fluid fills the inner region of the crack from the injection point to the fluid–fluid interface at $r = R_I$. Both regions are axisymmetric, as shown in figure 1.

2.1. *Fluid flow in the crack*

2.1.1. *Lubrication theory*

The low Reynolds number flow in the elongated fracture allows us to simplify the Navier–Stokes equation and use lubrication theory. The fluid is injected in a pre-formed crack whose aspect ratio is small:

$$w \ll R. \tag{2.1}$$

The Reynolds number of the flow through the crack is defined for the injected fluid as

$$Re = \epsilon \frac{\rho U w}{\mu} = \frac{\rho_{in} Q_{in}\, w(r=0)}{2\pi \mu_{in} R^2} \leq 1, \tag{2.2}$$

where ϵ is the aspect ratio of the crack. As a result, the flow of both fluids can be modelled with the lubrication theory, similarly to the single-phase flows in a penny-shaped fracture (Savitski & Detournay 2002; Detournay 2004; Detournay & Peirce 2014; Lai *et al.* 2015; O'Keeffe *et al.* 2018*a*). For the two-fluid system, the lubrication equations are

$$\frac{\partial w(r,t)}{\partial t} = \frac{1}{12\mu_{in}} \frac{1}{r} \frac{\partial}{\partial r}\left(r\, w^3(r,t)\, \frac{\partial p}{\partial r}\right) \quad \text{for } 0 \leq r \leq R_I, \tag{2.3}$$

$$\frac{\partial w(r,t)}{\partial t} = \frac{1}{12\mu_{0}} \frac{1}{r} \frac{\partial}{\partial r}\left(r\, w^3(r,t)\, \frac{\partial p}{\partial r}\right) \quad \text{for } R_I \leq r \leq R. \tag{2.4}$$

2.1.2. *Liquid interface*

The interface between the two fluids moves outwards during the injection and is described by the dynamics boundary condition

$$\begin{aligned} &\boldsymbol{n} \cdot \left(-p^- \boldsymbol{I} + \mu_{in}\left(\nabla \boldsymbol{u}^- + (\nabla \boldsymbol{u}^-)^{\mathrm{T}}\right)\right) \cdot \boldsymbol{n} + \gamma \kappa_c \\ &\quad = \boldsymbol{n} \cdot \left(-p^+ \boldsymbol{I} + \mu_{0}\left(\nabla \boldsymbol{u}^+ + (\nabla \boldsymbol{u}^+)^{\mathrm{T}}\right)\right) \cdot \boldsymbol{n}, \end{aligned} \tag{2.5}$$

where $\boldsymbol{n} = \boldsymbol{e}_r$ is the vector normal to the interface, and κ_c is the sum of the principal curvatures of the interface. The $+$ and $-$ exponents indicate that the value of the variable is determined at $r = R_I + \delta$ and $r = R_I - \delta$ respectively, with $\delta \ll R_I$. We note that

$\boldsymbol{\tau} = \mu(\boldsymbol{\nabla u} + (\boldsymbol{\nabla u})^{\mathrm{T}})$. We assume that the fluids are perfectly wetting the gel, and neglect the thin film deposited by the outer fluid. The normal stress balance is

$$p^- - p^+ = \sigma_I = \gamma\left(\frac{1}{R_I} + \frac{2}{w_I}\right) - \boldsymbol{n}\cdot\left(\boldsymbol{\tau}^+ - \boldsymbol{\tau}^-\right)\cdot\boldsymbol{n}$$
$$= \gamma\left(\frac{1}{R_I} + \frac{2}{w_I}\right) - 2\mu_0\left.\frac{\partial u}{\partial r}\right|_{r=R_I^+} - 2\mu_{in}\left.\frac{\partial u}{\partial r}\right|_{r=R_I^-}, \tag{2.6}$$

where w_I is the width of the fracture at the interface. The expression can be simplified further as $R_I > w_I$, and the viscous normal stresses are negligible. Indeed, the capillary number of the invading fluid is

$$Ca_{in} = \frac{\mu_{in}U}{\gamma} = \frac{\mu_{in}Q_{in}}{2\gamma\,\pi R\,w(r=0)} \ll 1. \tag{2.7}$$

The pressure change across the interface is

$$p^- - p^+ \approx \frac{2\gamma}{w_I}. \tag{2.8}$$

As the fluid–fluid interface moves, we can write the following kinematic condition using Reynolds equations:

$$q^- = q^+ = -\frac{w_I^3}{12\mu_{in}}\left.\frac{\partial p}{\partial r}\right|_{r=R_I^-} = -\frac{w_I^3}{12\mu_0}\left.\frac{\partial p}{\partial r}\right|_{r=R_I^+}. \tag{2.9}$$

2.1.3. *Volume conservation*

Finally, through volume conservation, the volume of the crack is equal to the volume injected. We note that V_0, the volume of the pre-fracture, is equal to the volume of the outer fluid. The injection begins at $t = 0$:

$$V_0 + Q_{in}t = 2\pi\int_0^R r\,w(r,t)\,\mathrm{d}r \tag{2.10}$$

and

$$Q_{in}t = 2\pi\int_0^{R_I} r\,w(r,t)\,\mathrm{d}r. \tag{2.11}$$

2.2. *Fracture equations*

2.2.1. *Linear elasticity*

Similarly to the single-fluid fracture (Savitski & Detournay 2002), the linear elasticity equation is

$$w(r,t) = \frac{8(1-\nu^2)R}{\pi E}\int_{r/R}^1 \frac{\xi}{\sqrt{\xi^2 - (r/R)^2}}\int_0^1 \frac{x\,p(x\xi R,t)}{\sqrt{1-x^2}}\,\mathrm{d}x\,\mathrm{d}\xi. \tag{2.12}$$

Parameter	Inner region	Outer region
Radius	$r = R_I\hat{r}$	$r = R\tilde{r}$
Width	$w = W_0\hat{w}$	$w = W_0\hat{w}$
Pressure	$p = P_0\hat{p}$	$p = P_0\hat{p}$

Table 1. Rescaled parameters.

2.2.2. *Fracture propagation*

In a small region at the tip of the crack, the material undergoes plastic deformation. The tensile fracture propagates when the mode I stress intensity factor K_I reaches a critical value called the toughness of the material, $K_{IC} = \sqrt{2E'\gamma_S}$, where γ_S is the fracture surface energy of the solid material (Kanninen & Popelar 1985), and $E' = E/(1-\nu^2)$. For a penny-shaped crack, the stress intensity factor near the tip is defined as (Rice 1968)

$$K_I = \frac{2}{\sqrt{\pi R}} \int_0^{R(t)} \frac{p(r,t)}{\sqrt{R^2 - r^2}}\, r\, \mathrm{d}r. \tag{2.13}$$

2.3. *Boundary conditions at the fracture tip and injection point*

At the tip of the crack, the width $w(R)$ goes to zero,

$$w = 0, \quad r = R(t), \tag{2.14a,b}$$

and the flow rate also goes to zero,

$$w^3(r,t)\,\frac{\partial p(r,t)}{\partial r} = 0, \quad r = R(t). \tag{2.15a,b}$$

At the point source, the local flow rate is equal to the injected flow rate:

$$2\pi \lim_{r\to 0} r\, q(r,t) = Q_{in}. \tag{2.16}$$

3. Scaling

The equations are non-dimensionalized by identifying the characteristic scales in both phases as listed in table 1.

The characteristic radius and aperture of the fracture are R and W_0, respectively, with R the radius of the fracture, and W_0 the maximum aperture of the fracture at $r = 0$. The position of the interface is R_I. The characteristic pressure in both the fluids is taken to be P_0. We define effective material parameters μ', E' and K' as proposed by Savitski & Detournay (2002):

$$\mu'_{in} = 12\mu_{in}, \quad \mu'_0 = 12\mu_0, \quad K' = 4\left(\frac{2}{\pi}\right)^{1/2} K_{IC} \quad \text{and} \quad E' = \frac{E}{1-\nu^2}. \tag{3.1a–d}$$

To compare the viscosity of the two liquids, we introduce the parameter $M = \mu'_{in}/\mu'_0$. When the two fluids are present in the fracture, we used a weighted average to define the resulting viscosity μ_e and the corresponding effective value $\mu'_e = 12\mu_e$.

Using the characteristic parameters summarized in table 1 and the effective material properties, we obtain the following set of equations to describe the displacement flow and fracture propagation.

(i) Lubrication theory (from (2.3) and (2.4)):

$$\frac{\mu_e' R^2}{W_0^2 P_0}\frac{\partial \hat{w}}{\partial t} = \frac{1}{\hat{r}}\frac{\partial}{\partial \hat{r}}\left(\hat{r}\hat{w}^3\frac{\partial \hat{p}}{\partial \hat{r}}\right). \tag{3.2}$$

(ii) Linear elasticity (from (2.12)):

$$\hat{w} = \frac{8R}{\pi E' W_0}\left[P_0\int_0^1\int_0^1 \frac{x\,\hat{p}(x\xi R, t)}{\sqrt{1-x^2}}\,\mathrm{d}x\,\mathrm{d}\xi\right]. \tag{3.3}$$

(iii) Fracture propagation (from (2.13)):

$$\frac{K'}{P_0\sqrt{R}} = \frac{2^{7/2}}{\sqrt{\pi}}\int_0^1 \frac{\tilde{p}\tilde{r}}{\sqrt{1-\tilde{r}^2}}\,\mathrm{d}\tilde{r}. \tag{3.4}$$

(iv) Global mass balance (from (2.10) and (2.11)):

$$\frac{Q_{in}t}{2\pi R_I^2 W_0} = \int_0^1 \hat{r}\hat{w}\,\mathrm{d}\hat{r} \tag{3.5}$$

and

$$\frac{V_0}{2\pi R^2 W_0} = \int_0^1 \tilde{r}\hat{w}\,\mathrm{d}\tilde{r} - \left(\frac{R_I}{R}\right)^2\int_0^1 \hat{r}\hat{w}\,\mathrm{d}\hat{r}. \tag{3.6}$$

As the fluid is injected, the elastic pressure drives the propagation of the crack, which is resisted by the viscous dissipation associated with the motion of the injected and displaced fluids, and the fracture toughness. We first assume that the interfacial pressure is negligible compared to the viscous and toughness-related stresses. We then assume that one of the resisting stresses controls the propagation and balances the elastic stress. Studies on single-fluid injection have validated this approach, with experimental evidence of the two asymptotic regimes. If the viscous stresses in the fluids are larger than the fracture-opening stress, then the fracture propagation is said to be in the viscous regime. Alternatively, the propagation is in the toughness regime. For both regimes, we can derive scaling arguments from the dimensionless groups derived from (3.2)–(3.6).

3.1. *Toughness regime*

For the toughness scaling, we set the non-dimensional groups in (3.3)–(3.6) equal to 1. Indeed, the viscous stresses are negligible, and the crack opening is limited by the toughness of the material. The scaling relations are

$$\frac{W_0 E'}{P_0 R} = 1, \tag{3.7}$$

$$\frac{K'}{P_0\sqrt{R}} = 1, \tag{3.8}$$

$$\frac{Q_{in}t}{R_I^2 W_0} = 1, \tag{3.9}$$

$$\frac{V_0}{W_0} = R^2 - R_I^2. \tag{3.10}$$

We define the characteristic time scale $T = V_0/Q_{in}$ and the corresponding dimensionless time $\tilde{t} = t/T$. By combining those groups, we obtain the toughness-dominated scaling of

the fracture properties:

$$W_0 = \left(\frac{K'}{E'}\right)^{4/5} V_0^{1/5} \left(1+\tilde{t}\right)^{1/5}, \tag{3.11}$$

$$R = \left(\frac{E'V_0}{K'}\right)^{2/5} \left(1+\tilde{t}\right)^{2/5}, \tag{3.12}$$

$$R_I = \left(\frac{E'V_0}{K'}\right)^{2/5} \tilde{t}^{1/2} \left(1+\tilde{t}\right)^{-1/10} \tag{3.13}$$

and

$$P_0 = K' \left(\frac{K'}{E'V_0}\right)^{1/5} \left(1+\tilde{t}\right)^{-1/5}. \tag{3.14}$$

3.2. *Viscous regime*

For the viscous scaling, we set the non-dimensional groups in (3.2)–(3.3) and (3.5)–(3.6) equal to 1. Here, the propagation of the fluids follows the lubrication equation, and the viscous dissipation limits the propagation of the fracture:

$$\frac{W_0 E'}{P_0 R} = 1, \tag{3.15}$$

$$\frac{\mu_e' R^2}{W_0^2 P_0 \left(t + V_0/Q_0\right)} = 1, \tag{3.16}$$

$$\frac{Q_{in} t}{R_I^2 W_0} = 1, \tag{3.17}$$

$$\frac{V_0}{W_0} = R^2 - R_I^2. \tag{3.18}$$

We define the effective viscosity of the volume of fluid in the fracture as a weighted average. The effective viscosity depends on the viscosities of the two fluids in the fracture and their relative volumes at time $\tilde{t}$:

$$\mu_e' = \frac{\mu_0' + \mu_{in}' \tilde{t}}{1+\tilde{t}}. \tag{3.19}$$

We obtain the viscous-dominated scaling of the variables:

$$W_0 = \left(\frac{\mu_e' Q_{in}}{E'}\right)^{2/9} V_0^{1/9} \left(1+\tilde{t}\right)^{1/3} \left(\alpha+\tilde{t}\right)^{-2/9}, \tag{3.20}$$

$$R = \left(\frac{E'}{\mu_e' Q_{in}}\right)^{1/9} V_0^{4/9} \left(1+\tilde{t}\right)^{1/3} \left(\alpha+\tilde{t}\right)^{1/9}, \tag{3.21}$$

$$R_I = \left(\frac{E'}{\mu_e' Q_{in}}\right)^{1/9} V_0^{4/9} \tilde{t}^{1/2} \left(1+\tilde{t}\right)^{-1/6} \left(\alpha+\tilde{t}\right)^{1/9}, \tag{3.22}$$

$$P_0 = \left(\frac{\mu_e' Q_{in} E'^2}{V_0}\right)^{1/3} \left(\alpha+\tilde{t}\right)^{-1/3}, \tag{3.23}$$

with $\alpha = Q_{in}/Q_0$. The results are summarized in table 2.

Fracture	Viscous regime	Toughness regime
Radius	$R \approx \left(\frac{E'}{\mu'_e Q_{in}}\right)^{1/9} V_0^{4/9}(1+\tilde{t})^{1/3}(\alpha+\tilde{t})^{1/9}$	$R \approx \left(\frac{E'V_0}{K'}\right)^{2/5}(1+\tilde{t})^{2/5}$
Interface	$R_I \approx \left(\frac{E'}{\mu'_e Q_{in}}\right)^{1/9} V_0^{4/9}\tilde{t}^{1/2}(1+\tilde{t})^{-1/6}(\alpha+\tilde{t})^{1/9}$	$R_I \approx \left(\frac{E'V_0}{K'}\right)^{2/5}\tilde{t}^{1/2}(1+\tilde{t})^{-1/10}$
Aperture	$W_0 \approx \left(\frac{\mu'_e Q_{in}}{E'}\right)^{2/9} V_0^{1/9}(1+\tilde{t})^{1/3}(\alpha+\tilde{t})^{-2/9}$	$W_0 \approx \left(\frac{K'}{E'}\right)^{4/5} V_0^{1/5}(1+\tilde{t})^{1/5}$

Table 2. Scaling relations for a penny-shaped fracture driven by a displacement flow. The time evolution of the geometrical properties of the fracture depends on the dominant resisting stress, which can be viscous or toughness-related.

3.3. *Discussion*

We consider the single-fluid limit of the two asymptotic regimes. Indeed, for a pre-fracture volume equal to zero, $V_0 = 0$, or for large values of the injection time $t \gg 1$, the expressions derived above should be equal to those obtained previously for single-fluid injection. In the toughness regime, we recover the single-fluid scaling relations (Savitski & Detournay 2002; Lai *et al.* 2016; O'Keeffe *et al.* 2018*a*)

$$W_0 = \left(\frac{K'}{E'}\right)^{4/5} (Q_{in}t)^{1/5}, \tag{3.24}$$

$$R = \left(\frac{E'}{K'}\right)^{2/5} (Q_{in}t)^{2/5} \tag{3.25}$$

and

$$P_0 = K' \left(\frac{K'}{E'Q_{in}t}\right)^{1/5}. \tag{3.26}$$

In the viscous regime, we also recover the scaling relations for a single-fluid injection:

$$W_0 = \left(\frac{\mu'_{in}}{E'}\right)^{2/9} Q_{in}^{1/3} t^{1/9}, \tag{3.27}$$

$$R = \left(\frac{E'}{\mu'_{in}}\right)^{1/9} Q_{in}^{1/3} t^{4/9} \tag{3.28}$$

and

$$P_0 = \left(\frac{\mu'_{in} E'^2}{t}\right)^{1/3}. \tag{3.29}$$

The fluid and matrix properties determine whether the fracture propagation is in the viscous or toughness regime. Past studies in single-fluid injection have defined criteria to predict the propagation regime. The regime is defined by the largest of the two stresses that oppose the elastic stress: the toughness-related stress $\Delta P_m \approx K'/\sqrt{R}$, and the viscous stress $\Delta P_v = \mu' Q/W_0^3$. In the viscous regime, we can use the scaling relations for R and

W_0 to estimate the ratio:

$$\left(\frac{\Delta P_m}{\Delta P_v}\right)_v = \left(\frac{K'^9 t}{E'^{13/2} Q^{3/2} \mu'^{5/2}}\right)^{1/9} = \left(\frac{t}{t_{mk}}\right)^{1/9} = \kappa, \tag{3.30}$$

where

$$t_{mk} = \left(\frac{E'^{13/2} Q^{3/2} \mu'^{5/2}}{K'^9}\right) \tag{3.31}$$

is the characteristic time scale of the system, and κ is the dimensionless toughness. Similarly, we can define the relative magnitude of both stresses in the toughness regime using the corresponding scaling relations:

$$\left(\frac{\Delta P_m}{\Delta P_v}\right)_m = \left(\frac{t}{t_{mk}}\right)^{2/5} = \kappa^{18/5}. \tag{3.32}$$

The viscous-dominated propagation is therefore associated with small values of κ, i.e. κ or $t/t_{mk} \lesssim 1$, and the toughness-dominated dynamics for κ or $t/t_{mk} \gg 1$.

Similarly, we can define the propagation regime of the fracture formed by a displacement flow. The toughness-related stress remains $\Delta P_m \approx K'/\sqrt{R}$, while the viscous stress becomes $\Delta P_v = \mu'_e Q_{in} R^2 (R_I^2 W_0^3 + \alpha V_0 W_0^2)^{-1}$ as defined in (3.8) and (3.16).

In the viscous regime, we substitute R, R_I and W_0 by the scaling relations defined in table 2:

$$\left(\frac{\Delta P_m}{\Delta P_v}\right)_v = \frac{K' V_0^{1/9} (\alpha + \tilde{t})^{5/18}}{E'^{13/18} \mu_e'^{5/18} Q_{in}^{5/18} (1 + \tilde{t})^{1/6}}. \tag{3.33}$$

Similarly, in the toughness regime, we estimate the ratio to be

$$\left(\frac{\Delta P_m}{\Delta P_v}\right)_m = \left(\frac{\Delta P_m}{\Delta P_v}\right)_v^{18/5}. \tag{3.34}$$

The ratio of the viscous and toughness-related stresses is a function of time that increases as $\tilde{t}^{1/9}$ for large values of $\tilde{t}$. In consequence, the propagation becomes toughness-controlled for long-time or large-volume injections. This result is consistent with what is known for a single-fluid injection. Contrary to the single-fluid criterion however, there is no explicit solution for the threshold injection time in the case of displacement flow. We can determine the propagation regime at time $\tilde{t}$ by comparing the pressure ratio with 1.

4. Experiments

Laboratory-scale experiments commonly use hydrogels as rock analogues to study hydraulic fracturing in brittle elastic materials (O'Keeffe & Linden 2017; Baumberger & Ronsin 2020). In particular, gelatin is a clear gel whose elasticity can be tuned easily by varying the volume fraction of gelatin powder in water (Giuseppe *et al.* 2009; Kavanagh *et al.* 2013; Lai *et al.* 2015). Because gelatin expands as it sets in the container, the material is spontaneously compressed, which furthers the analogy with soft rocks for fracture studies.

Exp.		Gel E (kPa)	Pre-fracture - oil-filled			Injection		
			μ_0 (Pa s)	Q_0 (ml min^{-1})	V_0 (ml)	Fluid	μ_{in} (Pa s)	Q_{in} (ml min^{-1})
1	○	30	0.01	0.3	5.6	Water	0.001	0.5
2	◀	30	0.01	0.3	6.2	Water	0.001	1
3	▲	30	0.01	0.15	5.1	Water	0.001	0.15
4	▶	30	0.01	0.15	6.3	Water	0.001	1
5	▼	15	0.02	0.1	7.1	Water	0.001	0.25
6	◆	30	0.01	0.3	3.9	Water	0.001	1.8
7	×	30	0.01	0.15	4	Water	0.001	1.8
8	■	30	0.01	0.5	6.2	Water	0.001	3.6
9	+	30	0.01	0.15	2.9	Water	0.001	0.54
10	▷	15	0.01	0.25	6.1	Water	0.001	0.5
11	✳	88	10.26	10	10	Glycerol	1.2	10
12	□	88	10.26	10	15	Glycerol/water	0.3	10
13	●	88	10.26	10	15	Glycerol	1.2	10
14	△	88	10.26	10	5	Glycerol	1.2	10
15	★	88	10.26	10	6.5	Syrup	8.6	10
16	◀	88	10.26	10	8	Syrup	8.6	10

Table 3. List of experiments: symbols and parameters.

4.1. *Material preparation and characterization*

The properties of the gelatin and the injected fluids control the fracture dynamics and are therefore characterized systematically. The gelatin is prepared by first heating ultra-pure water to 60 °C. While stirring the heated water, we slowly add gelatin powder (Gelatin type A; Sigma-Aldrich, USA) at a mass fraction of 10 % to 30 % to vary Young's modulus of the resulting gel. The gelatin then cools down to room temperature and sets over 24 hours prior to testing or fracturing. The Young's modulus of gelatin is measured with a custom-built displacement-controlled load frame. The sample is compressed by a ballscrew stage whose speed is set by a stepper motor Parker Compumotor OS22B controlled by a controller Parker Compumotor ZL6104. A load cell, Eaton 3108-10 (10 lb capacity) measures the force generated by the compressed sample. We record force–displacement values for cylindrical samples of gelatin of diameter and height equal to 1 in, and compute the stress–strain curves of the material. At small strain, all gelatin samples exhibit a linear elastic response to the compression. As listed in table 3, Young's modulus ranges between 15 and 116 kPa with a measurement error of ±10 %. The fracture energy and Poisson's ratio of the gelatin are assumed constant in our experiments, with $\gamma_S \approx 1$ J m^{-2} and $\nu \approx 0.5$ (Menand & Tait 2002).

To study displacement flows in fluid-filled fractures, we use immiscible Newtonian liquids. Silicone oils of different viscosity are used to form the pre-fracture. An aqueous solution composed of water, glycerol or corn syrup is then injected. The silicone oil is displaced outwards, further expanding the fracture in the gelatin. We measure the viscosity of the fluids and the surface tension at the oil/water and oil/syrup interfaces. Viscosity measurements are conducted using an MCR 92 Anton Parr rheometer with a parallel plate measuring system at 20 °C. The values obtained have a measurement error of ±1 % and are listed in table 3. Surface tension measurements are conducted using the pendant drop method with an Attension Theta Flex tensiometer: the surface tension

between silicone oil and water is $\gamma_{o/w} \approx 35 \pm 2$ mN m^{-1}, and between silicone oil and syrup is $\gamma_{o/s} \approx 50 \pm 2$ mN m^{-1}. The fluid properties are selected to study the propagation of the pre-fracture and fracture in a single regime during the experiment. For example, the values of κ at the end of the injection forming the pre-fracture, for experiments 1–10, vary as $35 \leq \kappa \leq 55$. Those experiments are expected to be in the toughness-dominated regime. Similarly, for experiments 11–16, $1.7 \leq \kappa \leq 1.9$ at the end of the formation of the pre-fracture: these experiments target the viscous-dominated propagation. These values are consistent with previous work on the formation of fluid-driven fractures in a block of gelatin. During the formation of the fracture through the displacement flow, we estimate the pressure ratio in the viscous regime $(\Delta P_m/\Delta P_v)_v$ at the end of the injection. The ratio varies between 24 and 58 for experiments 1–10, which are therefore expected to be in the toughness regime. The ratio varies between 1.9 and 2.5 for experiments 11–16, which are therefore expected to be in the viscous regime.

4.2. *Set-up*

The injection experiments are conducted in a large block of gelatin to avoid boundary effects on the propagation of the fracture. The gelatin is set in a cubic clear container (15 cm × 15 cm × 15 cm) around a blunt needle as represented in figure 2(*a*). We use a thin needle (inner diameter $ID = 1$ mm) for low-viscosity injections, and a wider needle for high-viscosity injections ($ID = 2.15$ mm). In our system, the fracture propagates horizontally, in the direction that opposes the least resistance. To avoid small tilts of the fracture that would compromise the quality of the recording, a plastic washer (outer diameter $OD = 6.5$ mm) is placed at the tip of the needle to initiate the fracture in the horizontal plane. Two fluids are successively pumped into the gelatin. For each fluid, we use a kdScientific® Legato 200 syringe pump to set the injection flow rate at a value between 0.1 and 20 ml min^{-1} with accuracy ±0.35 %. Both fluid-filled syringes are connected to the same injection needle using a switch valve. First, a silicone oil of viscosity μ_0 is injected at a constant volumetric flow rate Q_0 in the gelatin matrix to form the pre-fracture. The injection stops when a volume V_0 of silicone oil has been dispensed. The valve is then switched to inject the aqueous phase of viscosity μ_{in} into the pre-fracture at flow rate Q_{in}. The injection stops when the fracture tip is within 2 cm of the container walls to avoid confinement effects (Bunger, Gordeliy & Detournay 2013). The two fluids are dyed to allow visualizing the propagation of the fracture and interface between the two liquids in the clear gelatin: we use a blue water-based food dye for the aqueous phase, and a red oil-based food dye for the oil phase, as shown in figure 2. The propagation is recorded using a Nikon D5300 camera with a Phlox® LED panel ensuring uniform backlighting. The images are processed using a custom-made MATLAB code to determine the radius of the fracture R and the position of the interface between the two liquids R_I.

4.3. *Measurement of the fracture width*

To measure the thickness of the fracture during the propagation, we use a light absorption method (Bunger 2006; Bunger & Detournay 2008). This method consists in selecting a soluble dye and the corresponding optical filter. The filter should transmit light to the camera at the wavelength at which the dye absorbance A is maximum, A_λ. The absorbance follows Beer's law:

$$A_\lambda = -\log_{10}\left(\frac{I_\lambda}{I_{\lambda,0}}\right) = \epsilon_\lambda c h, \tag{4.1}$$

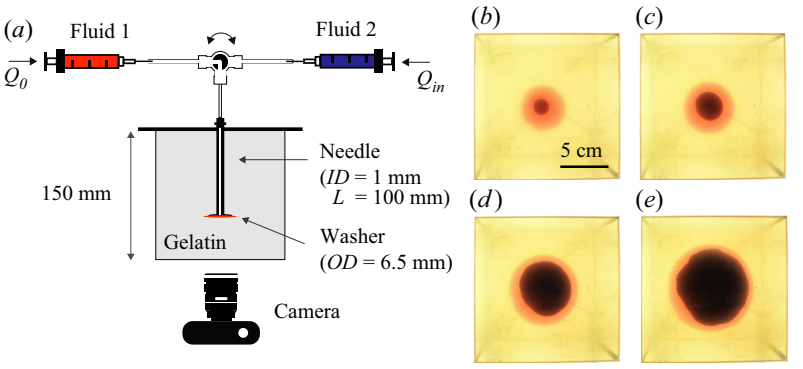

Figure 2. (*a*) Schematic of the experimental set-up. (*b–e*) Time evolution of the fracture formed in experiment 1. The water dyed with blue food colour is injected at $Q_{in} = 0.5$ ml min^{-1} in a pre-fracture formed with silicone oil dyed with red food colour. The recording starts when the water injection begins, and the experimental images are taken at (*b*) $t = 50$ s, (*c*) $t = 300$ s, (*d*) $t = 1300$ s, and (*e*) $t = 2800$ s. Supplementary movies 1 and 2 (available at https://doi.org/10.1017/jfm.2022.954) show the complete time evolution of the pre-fracture and fracture, respectively.

where $I_{\lambda,0}$ is the background intensity, and I_λ is the intensity when light passes through a liquid layer of thickness h, with dye concentration c. The parameter ϵ_λ characterizes the absorbance of the dye at the selected wavelength and is obtained through calibration. To measure the thickness of both liquids in the fracture, we use two dyes, one water-soluble and one oil-soluble, and record the absorbance using a single optical filter. To get accurate measurements, we select dyes with a large absorbance at the same wavelength. In all experiments, the water-soluble dye is nigrosin (Sigma-Aldrich) at 0.05 g l^{-1}. Nigrosin is a black dye that absorbs at all wavelengths. We use different dyes depending on the viscosity of the silicone oils, because of their solubility limit. We dilute Sudan red (Sigma-Aldrich) in the low-viscosity silicone oils, i.e. 10 and 20 mPa s silicone oils, at 0.05 g l^{-1}, and Nile red (Sigma-Aldrich) in high-viscosity silicone oils, i.e. 10 300 and 30 000 mPa s silicone oils, at 0.2 g l^{-1}. For experiments with Sudan red in the oil phase and nigrosin in the aqueous phase, we use a 520 nm optical filter. When Nile red dyes the oil phase and nigrosin the aqueous phase, we use a 632 nm optical filter.

To measure the thickness of the fracture, we first conduct calibration experiments for each dye solution. For the low-viscosity solutions (water, 10 and 20 mPa s silicone oils), we use a glass wedge with an aperture that increases linearly from 0 to 10 mm, as shown in figure 3. The wedge is placed on the LED panel and the light intensity is obtained by taking a picture of the wedge with the optical filter mounted on the camera. The background intensity corresponds to an empty wedge. The light intensity of a liquid-filled wedge decreases as the thickness of the aperture increases (see figure 3*b*). The grey values are used to determine the absorbance as a function of the liquid thickness, as plotted in figure 3(c). Using a linear fit, we get $1/\epsilon_\lambda c = 47.2$ mm for Sudan red in oil, and $1/\epsilon_\lambda c = 32.6$ mm for nigrosin in water, for $\lambda = 520$ nm. For the high-viscosity samples, we use rectangular cells that are easier to fill. The cell thickness or height ranges from 0.3 to 3 mm. For each cell, we measure the background intensity of the empty cell and the intensity of the cell filled with the viscous fluid, i.e. syrup, or 10 000 or 30 000 mPa s silicone oil. We obtain the absorbance for a set of thickness values as shown in figure 3. Using a linear fit, we get $1/\epsilon_\lambda c = 56.5$ mm for Nile red in oil, and $1/\epsilon_\lambda c = 44$ mm for nigrosin in water, for $\lambda = 632$ nm. The fitting parameters obtained are then used to obtain

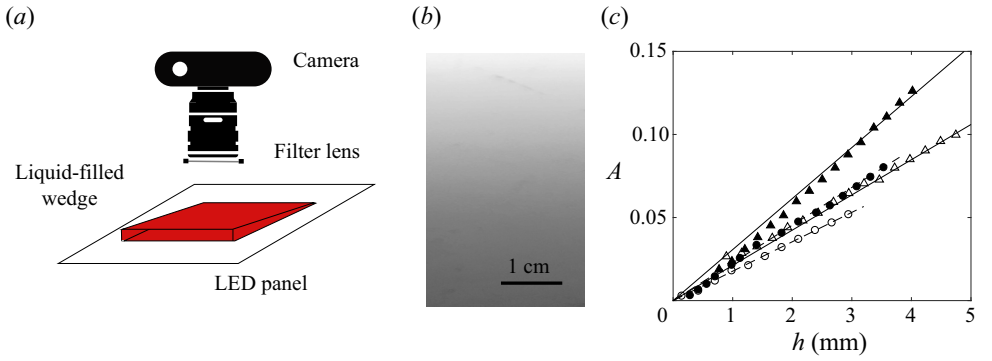

Figure 3. Calibration. (*a*) Schematic of the calibration experiment for low-viscosity fluids. (*b*) The intensity gradient was recorded for a wedge filled with water dyed with nigrosin at 0.05 g l^{-1} through the 520 nm filter. (*c*) Absorbance measured for nigrosin-dyed water at $\lambda = 520$ nm (▲), nigrosin-dyed syrup at $\lambda = 632$ nm (●), Sudan-red-dyed 10 mPa s siliconeoil at $\lambda = 520$ nm (△), and Nile-red-dyed 10 Pa s silicone oil at $\lambda = 632$ nm (○). The solid lines are the best linear fit for each calibration data set.

the width of the fracture using Beer's law:

$$h = \frac{A_\lambda}{\epsilon_\lambda c} = \frac{-\log_{10}\left(\dfrac{I_\lambda}{I_{\lambda,0}}\right)}{\epsilon_\lambda c}. \tag{4.2}$$

The concentrations of dyes chosen for this study, some of which are limited by solubility, are all sufficiently low for the absorbance to vary linearly with the sample thickness or fracture aperture. The accuracy of the measurements is limited by the noise due to low absorbance values.

5. Results

In this section, we present the results of the experiments listed in table 3. We measure the radius and aperture of the pre-fracture and fracture, and compare the data with the scalings obtained for the viscous and toughness regimes.

The fracture propagates radially upon injection of the fluid. Viscous fingering is not observed in our experiments, as illustrated in figures 2(*b–e*). The viscosity ratio $M = \mu_{in}/\mu_{out}$ varies between 0.05 and 1, and the thickness of the crack is of the order of a few millimetres, so the characteristic wavelength of the instability is larger than the perimeter of the injected fluid region. We estimate the experimental error by conducting an error analysis based on the scaling laws and the measurement error of the various parameters: 10 % for the Young's modulus E, 10 % for the fracture toughness K, 0.35 % for the flow rate Q, 1 % for the viscosity μ, and 5 % for the volume V_0. In the toughness regime, the experimental error on the radius is estimated to be ∼10 %. In the viscous regime, the error is ∼4 %.

5.1. *Single-fluid injection*

We prepare the pre-fracture by injecting silicone oil into the gelatin cube. After an initial pressure build-up, the oil propagates rapidly over the washer at the tip of the needle. A radial fracture then forms around the washer, propagating more slowly with the oil filling the gap between the two gelatin surfaces. The homogeneous properties of the gelatin result

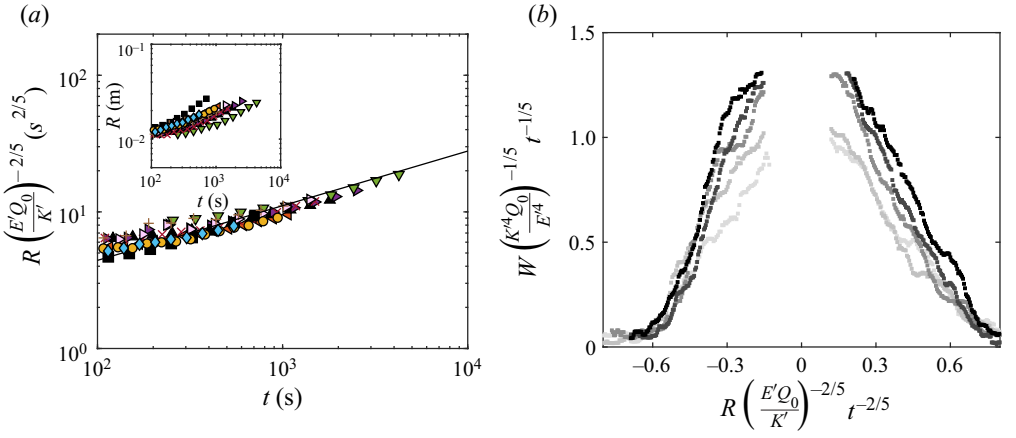

Figure 4. Dynamics of the pre-fracture for low-viscosity oils. (*a*) Dependence of rescaled fracture radius on time for experiments 1–10 (see table 3 for corresponding injection parameters). The radius is rescaled using (3.25) in the toughness scaling for single-fluid injection. The origin for time is set when the oil enters the gelatin. The black curve represents the best linear fit with slope 2/5. Inset: dependence of the radius R on time t. (*b*) Rescaled fracture thickness profiles based on (3.24) and (3.25) at $t = 245, 370, 495, 620, 745$ s, with time increasing from clear to dark grey. Experimental parameters: $E = 30$ kPa, $\mu_0 = 10$ mPa s, $Q_0 = 0.3$ ml min^{-1}.

in axisymmetric fractures for both low- and high-viscosity fluids. The radius of the fracture is measured during the injection and compared with the scaling for the toughness- and viscous-dominated regimes for a single fluid ((3.25) and (3.28), respectively). Experiments 1–10 are in the toughness regime as low-viscosity silicone oil is injected in soft gelatin (see table 3). Experiments 11–16 are in the viscous regime as high-viscosity silicone oil is injected in harder gelatin. In figure 4(*a*), we plot the results of the experiments in the toughness regime. The radius increases with time, and the rescaled radius follows a $t^{2/5}$ power law, which is consistent with (3.25). In the log-log scale, the best fit line with slope 2/5 has a prefactor $k = 0.7$, which is in agreement with the theoretical prefactor 0.85 derived by Savitski & Detournay (2002). These results are also consistent with previous experimental data in this regime (Lai *et al.* 2016; O'Keeffe *et al.* 2018*a*). In figure 5(*a*), we report the data obtained in the viscous regime. The experimental conditions for those experiments are similar, and the results demonstrate the high reproducibility of the experiments (Lecampion *et al.* 2017). The radius increases as a power law of time. Upon rescaling the radius with the viscous scaling parameter, the data collapse on a line of slope 4/9 with prefactor $k = 0.36$. This result differs from the theoretical prefactor 0.7, yet it is comparable to the values obtained in previous experimental studies in the viscous regime (Lai *et al.* 2015; O'Keeffe *et al.* 2018*a*). Due to the initiation transient and finite size of the container, the power-law fits span about a decade of the log-log plots, which is common for laboratory-scale experiments.

For each regime, we measure the fracture aperture using a dye whose absorbance varies linearly with the aperture. The results presented show the evolution of the fracture cross-section over time for one experiment in the toughness regime (see figure 4*b*) and one in the viscous regime (see figure 5*b*). For both experiments, the curves show the aperture as a function of the radial position at different injection times. Because the needle disturbs the absorbance measurement near the centre of the fracture, the aperture is not measured near the needle, i.e. for small values of the radius. Upon integration of the thickness curve recorded when the injection is complete, we obtain the value of $V_0 \pm 0.5$ ml.

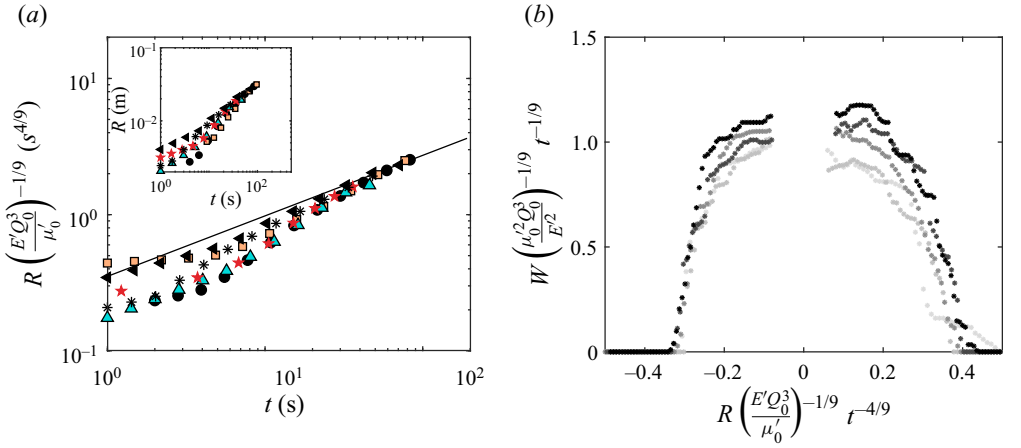

Figure 5. Dynamics of the pre-fracture for high-viscosity oils. (*a*) Dependence of rescaled fracture radius on time for experiments 11–16 (see table 3 for corresponding injection parameters). The radius is rescaled using (3.28) in the viscous scaling for single-fluid injection. The black curve represents the best linear fit with slope 4/9. Inset: dependence of the radius R on time t. (*b*) Rescaled fracture thickness profiles based on (3.27) and (3.28) at $t = 9, 11.5, 14, 16.5, 19$ s, with time increasing from clear to dark grey. Experimental parameters: $E = 88$ kPa, $\mu_0 = 10$ Pa s, $Q_0 = 10$ ml min^{-1}.

The aperture-radius curves are rescaled using the scaling for the aperture and radius. In both regimes, the curves collapse on a self-similar profile. The two data sets presented here are representative of the pre-fracture obtained for all the experiments conducted in this study, and are similar to results reported previously (Lai *et al.* 2016; O'Keeffe *et al.* 2018*a*).

5.2. *Displacement flow*

Once the pre-fracture is formed, the valve is immediately switched to the second immiscible to avoid further propagation of the pre-fracture (Möri & Lecampion 2021). The material properties of the gelatin contribute to the definition of the propagation regime. Low-stiffness gelatin allows the observation of the toughness regime, while the viscous regime is most commonly reached in stiffer hydrogel. Thus we characterize the displacement flow and fracture propagation in the toughness regime with the experimental systems 1–10 (see table 3), in which the pre-fracture is also formed in the toughness regime. The injected fluid is water. Similarly, we investigate the viscous regime in experiments 11–16. The displacing fluid is a syrup whose high viscosity is of the same magnitude as the silicone oil in the pre-fractures. During the displacement flow, the fracture continues its radial expansion but with a different dynamic from the one observed during the formation of the pre-fracture. To study the radial expansion of the fracture during the injection, we track the position of the interface between the two fluids, R_I, and the radius of the fracture, R, over time. In figure 6, we plot the results of the experiments in the toughness regime. The radial position of the interface increases with time, similarly to what was observed for a single-fluid injection. The annular region of displaced fluid between R_I and R moves outwards, and its radius $R - R_I$ decreases over time. Using the equations in table 2, we plot the rescaled radii with respect to the relevant dimensionless time on the log-log scale. The rescaled radial positions of the interface collapses on a line of slope 1 with prefactor 1. The rescaled radii of the fracture collapse on a line of slope 1

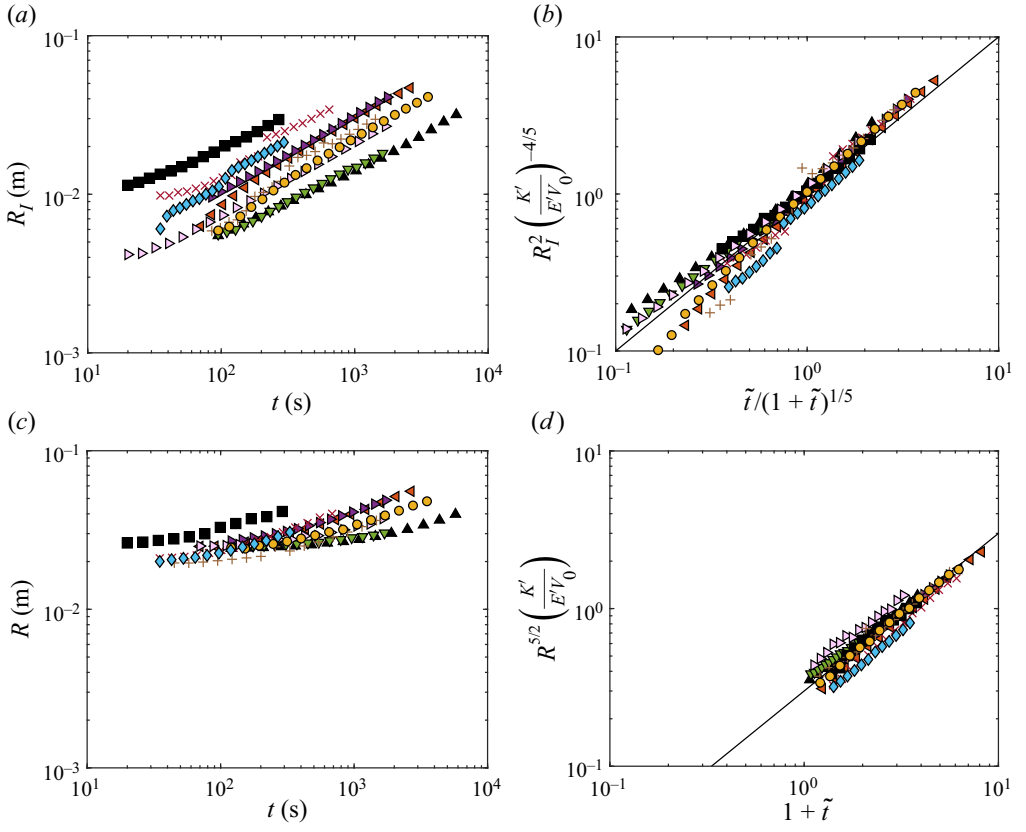

Figure 6. Dynamics of the fracture for the low-viscosity aqueous phase. (*a*) Dependence of the position of the interface on time for experiments 1–10 (see table 3 for corresponding injection parameters). (*b*) Rescaled interface position as a function of rescaled time, based on the toughness scaling laws in table 2. (*c*) Dependence of the fracture radius on time. (*d*) Rescaled radius as a function of rescaled time, based on the toughness scaling laws in table 2. The black curves represent the best linear fit with slope 1.

with prefactor 0.3. We note that for large values of time $\tilde{t} \gg 1$, the fracture dynamics for the displacement flow is expected to become similar to the fracture dynamics for a single fluid. Indeed, if we plot the dimensionless radius as $R^{5/2}(K'/E'V_0)$, then the prefactor 0.3 for the displacement flow is comparable with the prefactor for a single fluid $0.7^{5/2} \approx 0.4$. In figure 7, we plot the results of the displacement flow experiments in the viscous regime. The results can be rescaled using equations in the corresponding column of table 2. We plot the rescaled radii with respect to the relevant functions of the dimensionless time on the log-log scale. The rescaled radial positions of the interface collapse on a line of slope 1 with prefactor 0.37. The rescaled radii of the fracture collapse on a line of slope 1 with prefactor 0.36. We note that for large values of time $\tilde{t} \gg 1$, the fracture dynamics for the displacement flow is expected to become similar to the fracture dynamics for a single fluid. Since at large values of $\tilde{t}$, $(1+\tilde{t})^{1/3}(\alpha+\tilde{t})^{1/9} \approx \tilde{t}^{4/9}$, the identical prefactor for the scaling of the radius for the pre-fracture and the fracture indicates that indeed the single-fluid behaviour is recovered for large injection times. We also note that for large values of the fracture radius, the experimental data fall below the trend line. This is due to the slow down of the growth due to the confinement of the gelatin block.

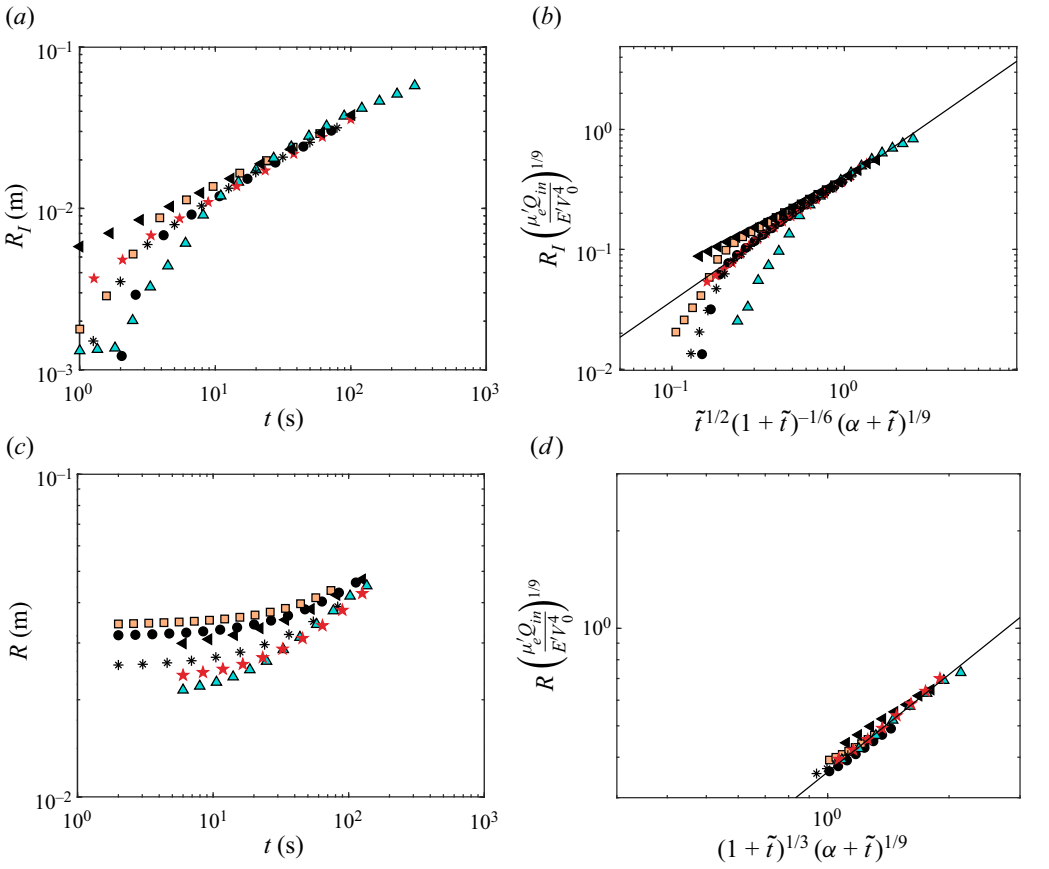

Figure 7. Dynamics of the fracture for the high-viscosity aqueous phase. (*a*) Dependence of the position of the interface on time for experiments 11–16 (see table 3 for corresponding injection parameters). (*b*) Rescaled interface position as a function of rescaled time, based on the viscous scaling laws in table 2. (*c*) Dependence of the fracture radius on time. (*d*) Rescaled radius as a function of the rescaled time, based on the viscous scaling laws in table 2. The black curves represent the best linear fit with slope 1.

Experimentally, this is associated with the tilting of the fracture and the formation of finger-like structures.

For the displacement flows, we measure the fracture aperture in the two fluids simultaneously, relying on two different dyes (see figures 8 and 9). Since the two dyes absorb the light differently, the absorbance profile presents a discontinuity across the interface. The absorbance values are converted to thickness measurements using Beer's law and the calibration parameters. The experimental results plotted in figures 8(*a*) and 9(*a*) show that the aperture is a continuous function of the radial position. The aperture–radius curves are rescaled using the scalings for both aperture and radius. In the toughness regime, both the rescaled aperture and radius collapse, resulting in overlapping profiles; see figure 8(*b*). In the viscous regime, the rescaled profiles collapse onto a single curve; see figure 9(*b*). The two data sets presented here are representative of all the experiments. In summary, the experimental observations establish the existence of two regimes and validate the respective scaling relations.

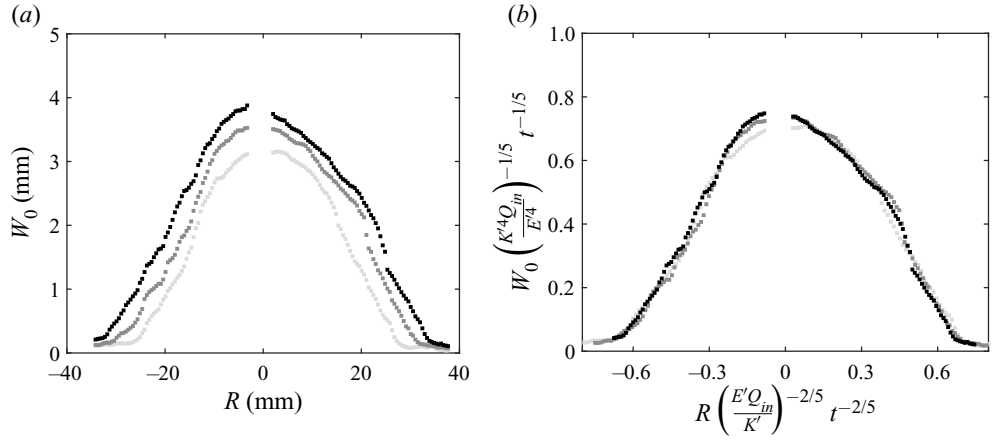

Figure 8. Fracture profile for the low-viscosity aqueous phase. (*a*) Fracture profiles at $t = 150, 250, 350$ s, with time increasing from clear to dark grey. (*b*) Rescaled fracture profiles using the toughness scaling laws in table 2. Experimental parameters: $E = 30$ kPa, $\mu_0 = 10$ mPa s, $Q_0 = 0.3$ ml min^{-1}, $V_0 = 2.5$ ml, $\mu_{in} = 1$ mPa s, $Q_{in} = 1.8$ ml min^{-1}.

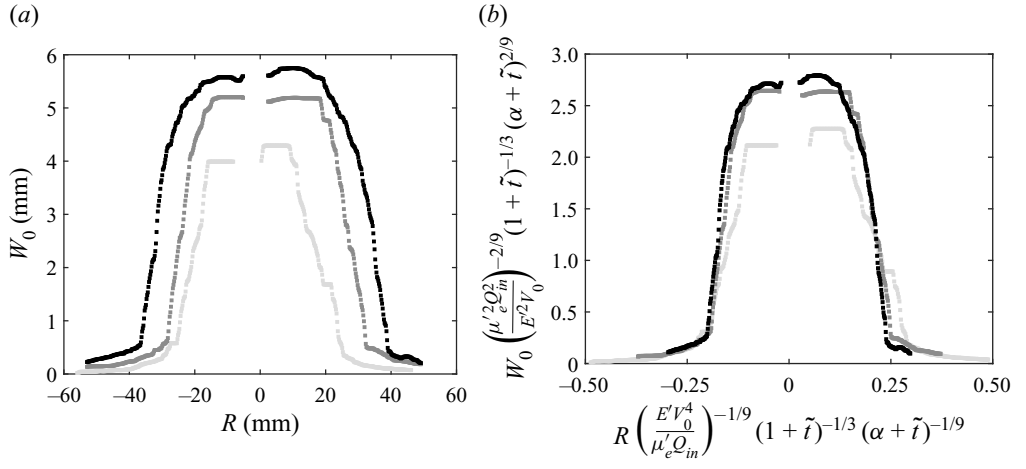

Figure 9. Fracture profile for the high-viscosity aqueous phase. (*a*) Fracture profiles at $t = 5, 10, 40$ s, with time increasing from clear to dark grey. (*b*) Rescaled fracture profiles using the viscous scaling laws in table 2. Experimental parameters: $E = 88$ kPa, $\mu_0 = 10$ Pa s, $Q_0 = 10$ ml min^{-1}, $V_0 = 8$ ml, $\mu_{in} = 8.6$ Pa s, $Q_{in} = 10$ ml min^{-1}.

6. Conclusion

In this study, we model the properties of fractures driven by displacement flows by revisiting the theoretical framework established for single-fluid injections. We derive scaling relationships for the position of the interface between the two fluids, the radius and the aperture of the fracture in a brittle elastic matrix in the viscous-dominated and toughness-dominated regimes. We define a dimensionless time, which is equal to the ratio of the volume of displacing fluid injected over the volume of the pre-fracture. In the toughness regime, the propagation dynamics is independent of the fluid properties. As a result, the fracture dynamics for the displacement flow is the same as the dynamics

for a single fluid, with the addition of initial finite volume V_0. In the viscous regime, however, the two fluids that fill the fracture contribute to the viscous dissipation. Over time, the relative volume of the two fluids changes. To describe the viscous dissipation in the fracture, we therefore define an average viscosity that accounts for the relative volume of displaced and displacing fluid. The scalings are compared to experimental results obtained by successively injecting an oil phase and an aqueous phase in a gelatin block. The experiments confirm the existence of two regimes of fracture propagation, and are in good agreement with the derived relationships.

This study focuses on displacement flows of immiscible fluids with comparable viscosities. Other types of displacement flows are common in fractures. For example, industrial applications involve the sequential injection of miscible aqueous fluids, some of which can be complex fluids such as suspensions of particles or polymer solutions. Recent and future efforts to characterize and model multiphase flows in fractures should ultimately support efficient hydraulic fracturing operations.

Supplementary movies. Supplementary movies are available at https://doi.org/10.1017/jfm.2022.954.

Acknowledgements. We would like to thank Z. Zheng for helpful discussions.

Funding. The work was supported in part by the ACS PRF (grant no. 60464-ND9).

Declaration of interests. The authors report no conflict of interest.

Data availability statement. The data associated with this paper can be downloaded from the repository https://doi.org/10.25349/D9W32D.

Author ORCIDs.
Emilie Dressaire https://orcid.org/0000-0002-4544-8736.

References

Al-Housseiny, T.T. & Stone, H.A. 2013 Controlling viscous fingering in tapered Hele-Shaw cells. *Phys. Fluids* **25** (9), 092102–12.

Al-Housseiny, T.T., Tsai, P.A. & Stone, H.A. 2012 Control of interfacial instabilities using flow geometry. *Nat. Phys.* **8** (10), 747–750.

Alessi, D.S., Zolfaghari, A., Kletke, S., Gehman, J., Allen, D.M. & Goss, G.G. 2017 Comparative analysis of hydraulic fracturing wastewater practices in unconventional shale development: water sourcing, treatment and disposal practices. *Can. Water Resour. J.* **42** (2), 1–17.

Bao, X. & Eaton, D.W. 2016 Fault activation by hydraulic fracturing in western Canada. *Science* **354** (6318), 1406–1409.

Barbati, A.C., Desroches, J., Robisson, A. & McKinley, G.H. 2016 Complex fluids and hydraulic fracturing. *Annu. Rev. Chem. Biomol. Engng* **7** (1), 415–453.

Barboza, B.R., Chen, B. & Li, C. 2021 A review on proppant transport modelling. *J. Petrol. Sci. Engng* **204**, 108753.

Barenblatt, G.I. 1956 On the formation of horizontal cracks in hydraulic fracture of an oil-bearing stratum. *Prikl. Mat. Mech.* **20**, 475–486.

Baumberger, T. & Ronsin, O. 2020 Environmental control of crack propagation in polymer hydrogels. *Mech. Soft Mater.* **2** (1), 14.

Bessmertnykh, A., Dontsov, E. & Ballarini, R. 2021 Semi-infinite hydraulic fracture driven by a sequence of power-law fluids. *J. Eng. Mech.* **147** (10), 04021064.

Bunger, A.P. 2006 A photometry method for measuring the opening of fluid-filled fractures. *Meas. Sci. Technol.* **17** (12), 3237.

Bunger, A.P. & Detournay, E. 2005 Asymptotic solution for a penny-shaped near-surface hydraulic fracture. *Engng Fract. Mech.* **72** (16), 2468–2486.

Bunger, A.P. & Detournay, E. 2008 Experimental validation of the tip asymptotics for a fluid-driven crack. *J. Mech. Phys. Solids* **56** (11), 3101–3115.

BUNGER, A.P., GORDELIY, E. & DETOURNAY, E. 2013 Comparison between laboratory experiments and coupled simulations of saucer-shaped hydraulic fractures in homogeneous brittle-elastic solids. *J. Mech. Phys. Solids* **61** (7), 1636–1654.

CAULK, R.A., GHAZANFARI, E., PERDRIAL, J.N. & PERDRIAL, N. 2016 Experimental investigation of fracture aperture and permeability change within enhanced geothermal systems. *Geothermics* **62**, 12–21.

CHEN, J.-D. 1989 Growth of radial viscous fingers in a Hele-Shaw cell. *J. Fluid Mech.* **201**, 223–242.

CHEN, Y.-F., FANG, S., WU, D.-S. & HU, R. 2017 Visualizing and quantifying the crossover from capillary fingering to viscous fingering in a rough fracture. *Water Resour. Res.* **53** (9), 7756–7772.

COTTIN, C., BODIGUEL, H. & COLIN, A. 2010 Drainage in two-dimensional porous media: from capillary fingering to viscous flow. *Phys. Rev.* E **82** (4), 046315.

CUETO-FELGUEROSO, L. & JUANES, R. 2013 Forecasting long-term gas production from shale. *Proc. Natl Acad. Sci. USA* **110** (49), 19660–19661.

DESROCHES, J., DETOURNAY, E., LENOACH, B., PAPANASTASIOU, P., PEARSON, J.R.A., THIERCELIN, M. & CHENG, A. 1994 The crack tip region in hydraulic fracturing. *Proc. R. Soc. Lond.* A **447** (1929), 39–48.

DETOURNAY, E. 2004 Propagation regimes of fluid-driven fractures in impermeable rocks. *Intl J. Geomech.* **4** (1), 35–45.

DETOURNAY, E. 2016 Mechanics of hydraulic fractures. *Annu. Rev. Fluid Mech.* **48** (1), 311–339.

DETOURNAY, E. & GARAGASH, D.I. 2003 The near-tip region of a fluid-driven fracture propagating in a permeable elastic solid. *J. Fluid Mech.* **494**, 1–32.

DETOURNAY, E. & PEIRCE, A. 2014 On the moving boundary conditions for a hydraulic fracture. *Intl J. Engng Sci.* **84**, 147–155.

GARAGASH, D.I. & DETOURNAY, E. 2000 The tip region of a fluid-driven fracture in an elastic medium. *Trans. ASME J. Appl. Mech.* **67** (1), 183–192.

GARAGASH, D.I. & DETOURNAY, E. 2005 Plane-strain propagation of a fluid-driven fracture: small toughness solution. *Trans. ASME J. Appl. Mech.* **72** (6), 916–928.

GIUSEPPE, E.D., FUNICIELLO, F., CORBI, F., RANALLI, G. & MOJOLI, G. 2009 Gelatins as rock analogs: a systematic study of their rheological and physical properties. *Tectonophysics* **473** (3–4), 391–403.

GLASS, R.J., RAJARAM, H. & DETWILER, R.L. 2003 Immiscible displacements in rough-walled fractures: competition between roughening by random aperture variations and smoothing by in-plane curvature. *Phys. Rev.* E **68** (6), 061110.

HOMSY, G.M. 1987 Viscous fingering in porous media. *Annu. Rev. Fluid Mech.* **19** (1), 271–311.

HORMOZI, S. & FRIGAARD, I.A. 2017 Dispersion of solids in fracturing flows of yield stress fluids. *J. Fluid Mech.* **830**, 93–137.

HUPPERT, H.E. & NEUFELD, J.A. 2013 The fluid mechanics of carbon dioxide sequestration. *Annu. Rev. Fluid Mech.* **46** (1), 255–272.

JIA, B., TSAU, J.-S. & BARATI, R. 2019 A review of the current progress of CO_2 injection EOR and carbon storage in shale oil reservoirs. *Fuel* **236**, 404–427.

KANNINEN, M.F. & POPELAR, C.H. 1985 *Advanced Fracture Mechanics*. Oxford Engineering Science Series, vol. 15. Oxford University Press.

KAVANAGH, J.L., MENAND, T. & DANIELS, K.A. 2013 Gelatine as a crustal analogue: determining elastic properties for modelling magmatic intrusions. *Tectonophysics* **582**, 101–111.

KHRISTIANOVIC, S.A. & ZHELTOV, Y.P. 1955 Formation of vertical fractures by means of highly viscous liquid. *4th World Petrol. Congr. Proc. OnePetro* **2**, 576–586.

LAI, C.-Y., RALLABANDI, B., PERAZZO, A., ZHENG, Z., SMIDDY, S.E. & STONE, H.A. 2018 Foam-driven fracture. *Proc. Natl Acad. Sci. USA* **115** (32), 8082–8086.

LAI, C.-Y., ZHENG, Z., DRESSAIRE, E. & STONE, H.A. 2016 Fluid-driven cracks in an elastic matrix in the toughness-dominated limit. *Phil. Trans. R. Soc. Lond.* A **374** (2078), 20150425.

LAI, C.-Y., ZHENG, Z., DRESSAIRE, E., WEXLER, J.S. & STONE, H.A. 2015 Experimental study on penny-shaped fluid-driven cracks in an elastic matrix. *Proc. R. Soc. Lond.* A **471** (2182), 20150255.

LECAMPION, B., DESROCHES, J., JEFFREY, R.G. & BUNGER, A.P. 2017 Experiments versus theory for the initiation and propagation of radial hydraulic fractures in low-permeability materials.. *J. Geophys. Res.* **122** (2), 1239–1263.

LENORMAND, R., TOUBOUL, E. & ZARCONE, C. 1988 Numerical models and experiments on immiscible displacements in porous media. *J. Fluid Mech.* **189**, 165–187.

LENORMAND, R., ZARCONE, C. & SARR, A. 1983 Mechanisms of the displacement of one fluid by another in a network of capillary ducts. *J. Fluid Mech.* **135**, 337–353.

LISTER, J.R. & KERR, R.C. 1991 Fluid-mechanical models of crack propagation and their application to magma transport in dykes. *J. Geophys. Res.* **96** (B6), 10049–10077.

LU, N.B., BROWNE, C.A., AMCHIN, D.B., NUNES, J.K. & DATTA, S.S. 2019 Controlling capillary fingering using pore size gradients in disordered media. *Phys. Rev. Fluids* **4** (8), 084303.

LUO, J., ZHU, Y., GUO, Q., TAN, L., ZHUANG, Y., LIU, M., ZHANG, C., XIANG, W. & ROHN, J. 2017 Experimental investigation of the hydraulic and heat-transfer properties of artificially fractured granite. *Sci. Rep.* **7** (1), 39882.

MENAND, T. & TAIT, S.R. 2002 The propagation of a buoyant liquid-filled fissure from a source under constant pressure: an experimental approach. *J. Geophys. Res.* **107** (B11), ECV 16-1-ECV 16–14.

MÖRI, A. & LECAMPION, B. 2021 Arrest of a radial hydraulic fracture upon shut-in of the injection. *Intl J. Solids Struct.* **219**, 151–165.

MOUKHTARI, F.-E. & LECAMPION, B. 2018 A semi-infinite hydraulic fracture driven by a shear-thinning fluid. *J. Fluid Mech.* **838**, 573–605.

MURPHY, H.D., TESTER, J.W., GRIGSBY, C.O. & POTTER, R.M. 1981 Energy extraction from fractured geothermal reservoirs in low-permeability crystalline rock. *J. Geophys. Res.* **86** (B8), 7145–7158.

O'KEEFFE, N.J., HUPPERT, H.E. & LINDEN, P.F. 2018*a* Experimental exploration of fluid-driven cracks in brittle hydrogels. *J. Fluid Mech.* **844**, 435–458.

O'KEEFFE, N.J. & LINDEN, P.F. 2017 Hydrogel as a medium for fluid-driven fracture study. *Exp. Mech.* **57** (9), 1483–1493.

O'KEEFFE, N.J., ZHENG, Z., HUPPERT, H.E. & LINDEN, P.F. 2018*b* Symmetric coalescence of two hydraulic fractures. *Proc. Natl Acad. Sci. USA* **115** (41), 10228–10232.

OSIPTSOV, A.A. 2017 Fluid mechanics of hydraulic fracturing: a review. *J. Petrol. Sci. Engng* **156**, 513–535.

PARISIO, F. & YOSHIOKA, K. 2020 Modeling fluid reinjection into an enhanced geothermal system. *Geophys. Res. Lett.* **47** (19), e2020GL089886.

PARK, C.-W. & HOMSY, G.M. 1984 Two-phase displacement in Hele-Shaw cells: theory. *J. Fluid Mech.* **139**, 291–308.

PATERSON, L. 1981 Radial fingering in a Hele-Shaw cell. *J. Fluid Mech.* **113** (1), 513–529.

PENG, G.G., PIHLER-PUZOVIC, D., JUEL, A., HEIL, M. & LISTER, J.R. 2015 Displacement flows under elastic membranes. Part 2. Analysis of interfacial effects. *J. Fluid Mech.* **784**, 512–547.

PIHLER-PUZOVIĆ, D., ILLIEN, P., HEIL, M. & JUEL, A. 2012 Suppression of complex fingerlike patterns at the interface between air and a viscous fluid by elastic membranes. *Phys. Rev. Lett.* **108** (7), 074502.

PIHLER-PUZOVIĆ, D., JUEL, A., PENG, G.G., LISTER, J.R. & HEIL, M. 2015 Displacement flows under elastic membranes. Part 1. Experiments and direct numerical simulations. *J. Fluid Mech.* **784**, 487–511.

PIHLER-PUZOVIĆ, D., PÉRILLAT, R., RUSSELL, M., JUEL, A. & HEIL, M. 2013 Modelling the suppression of viscous fingering in elastic-walled Hele-Shaw cells. *J. Fluid Mech.* **731**, 162–183.

PRIMKULOV, B.K., PAHLAVAN, A.A., FU, X., ZHAO, B., MACMINN, C.W. & JUANES, R. 2019 Signatures of fluid–fluid displacement in porous media: wettability, patterns and pressures. *J. Fluid Mech.* **875**, R4.

PRIMKULOV, B.K., PAHLAVAN, A.A., FU, X., ZHAO, B., MACMINN, C.W. & JUANES, R. 2021 Wettability and Lenormand's diagram. *J. Fluid Mech.* **923**, A34.

RICE, J.R. 1968 *Mathematical Analysis in the Mechanics of Fracture*. Academic Press.

RUBIN, A.M. 1995 Propagation of magma-filled cracks. *Annu. Rev. Earth Planet. Sci.* **23** (1), 287–336.

SAFFMAN, P.G. & TAYLOR, G.I. 1958 The penetration of a fluid into a porous medium or Hele-Shaw cell containing a more viscous liquid. *Proc. R. Soc. Lond.* A **245** (1242), 312–329.

SAVITSKI, A.A. & DETOURNAY, E. 2002 Propagation of a penny-shaped fluid-driven fracture in an impermeable rock: asymptotic solutions. *Intl J. Solids Struct.* **39** (26), 6311–6337.

SNEDDON, I.N. & MOTT, N.F. 1946 The distribution of stress in the neighbourhood of a crack in an elastic solid. *Proc. R. Soc. Lond.* A **187** (1009), 229–260.

SPENCE, D.A. & SHARP, P. 1985 Self-similar solutions for elastohydrodynamic cavity flow. *Proc. R. Soc. Lond.* A **400** (1819), 289–313.

STOKES, J.P., WEITZ, D.A., GOLLUB, J.P., DOUGHERTY, A., ROBBINS, M.O., CHAIKIN, P.M. & LINDSAY, H.M. 1986 Interfacial stability of immiscible displacement in a porous medium. *Phys. Rev. Lett.* **57** (14), 1718–1721.

TABELING, P., ZOCCHI, G. & LIBCHABER, A. 1987 An experimental study of the Saffman–Taylor instability. *J. Fluid Mech.* **177**, 67–82.

TAKADA, A. 1990 Experimental study on propagation of liquid-filled crack in gelatin: shape and velocity in hydrostatic stress condition. *J. Geophys. Res.* **95** (B6), 8471–8481.

TANVEER, S. 1993 Evolution of Hele-Shaw interface for small surface tension. *J. Geophys. Res.* **343** (1668), 155–204.

WANG, J., ELSWORTH, D. & DENISON, M.K. 2018 Propagation, proppant transport and the evolution of transport properties of hydraulic fractures. *J. Fluid Mech.* **855**, 503–534.

YANG, Z., MÉHEUST, Y., NEUWEILER, I., HU, R., NIEMI, A. & CHEN, Y.-F. 2019 Modeling immiscible two-phase flow in rough fractures from capillary to viscous fingering. *Water Resour. Res.* **55** (3), 2033–2056.

ZHAO, B., MACMINN, C.W. & JUANES, R. 2016 Wettability control on multiphase flow in patterned microfluidics. *Proc. Natl Acad. Sci. USA* **113** (37), 10251–10256.